Finite Volume TVD Scheme on Unstructured Grids for Space MHD Simulations and Space Weather

T. Tanaka[1]

Communications Research Lab., Koganei-shi, Tokyo 184-8795, Japan

Abstract. A three-dimensional (3-D) high-resolution magnetohydrodynamic (MHD) simulation scheme is developed on unstructured grid systems to solve the complex-system problems in space science and space weather in which numerical difficulties arise from inhomogeneity due to strong background potential fields, inclusion of multi-species ions, and formations of shocks and discontinuities. The ideal MHD equations are extended to the 9-component MHD equations for multi-component ions and modified so as to avoid a direct inclusion of background potential field in dependent variables through the use of new variables. The numerical scheme adopts the finite volume method (FVM) with an upwinding numerical flux based on the linearized Riemann solver. Upwindings on unstructured grid systems are realized from the fact that the MHD equations are symmetric with respect to the rotation of the space. Despite the modifications of the equation system, the eigenvectors in the mode-synthesis matrix necessary for the evaluation of the upwinding numerical flux can still be written analytically. To get a higher order of accuracy, the upwinding flux is extended to the third-order total variation diminishing (TVD) numerical flux in the calculation of FVM, through the monotonic upstream scheme for conservation laws (MUSCL) approach and Van Leer's differentiable limiter. Three numerical examples are given in order to show the efficiency of the above scheme.

1 Introduction

Recently, the magnetohydrodynamic (MHD) simulations are widely applied to many problems in space science with a great success [1] [2] [3] [4] [5] [6] [7] [8] [9] [10] [11] [12]. A rapid development of supercomputers in computational speed and memory size gives a conviction for further developments in this fruitful area. In these studies, the developments of supercomputers and numerical schemes are like the two wheels of a cart. In order to apply the MHD simulations to the problems having more complex configurations, further improvements of numerical schemes are also unavoidable. In this paper, we develop a numerical MHD scheme that enables an exact treatment of multi-scale space plasma including multi-component ions and strong background potential field, with an excellent capturing of shocks and discontinuities.

In the space science, we must always study the complex systems which are controlled by the coupling processes between different regions having quite different characteristics. Auroral physics is a typical example of this kind of problem [3] [5]. The main process controlling this problem is the coupling effects that occur between the magnetosphere and the ionosphere. The characteristic length and time scales of these two regions are vastly different. If numerical MHD simulations are applied to these problems, then it becomes necessary to assign different grid point densities to each region, in order to facilitate the simultaneous treatment of the different regions. Therefore, it is unavoidable to adopt an unstructured grid system. The ordinary finite difference method (FDM) which is widely used to solve differential equations numerically is no longer applicable on an unstructured grid system and so here we consider the finite volume method (FVM) based on the flux conservation law [13].

High-speed flowing plasma that is frequently treated in space science tends to form shocks and discontinuities. The use of standard numerical schemes of second-order accuracy (e.g. the Lax-Wendroff method) generates spurious oscillations at high gradients. Therefore, there is a need to use more advanced schemes that can adequately represent these shocks and discontinuities. An outstanding approach is to evaluate numerical flux in the FVM from an upwinding method based on the linearized Riemann solver [14] [15] [16]. To get a higher order of accuracy, the upwinding scheme for numerical flux is extended to the total variation diminishing (TVD) scheme. Among many TVD schemes, a third-order TVD scheme based on the monotonic upstream scheme for conservation laws (MUSCL) approach is considered in this paper [17] [18]. With this numerical flux, excellent shock-capturing is enabled along with stable and highly-accurate computations. The eigenvalues and eigenvectors of the MHD flux Jacobian matrix necessary for the upwinding calculations are derived from the well-known Alfven, fast and slow velocities [14]. The calculation of eigenvectors is done with special care when wave propagations become parallel or perpendicular to the ambient magnetic field, because degenerations of eigenvalues occur in these cases [14] [19].

Another problem in space science is that many planets and stars treated in the complex-system simulation have a strong dipole magnetic field generated in their interior regions. In the case of the earth, the magnitude of the dipole magnetic field is about 30000 nT in the ionospheric region near the Earth, while it diminishes rapidly in the magnetosphere to about 10 nT. Therefore, the magnitude of the intrinsic magnetic field varies over a wide range in the whole treating region, in the problem of magnetosphere-ionosphere (M-I) couplings. On the other hand, the variable components of magnetic field, which are calculated from the MHD equations, exhibit a similar magnitude over the whole region. As a result, the ratio of variable to intrinsic components of the magnetic field becomes extremely small in the ionospheric region. These situations give a difficulty in the numerical study of the coupling process between two different regions. Especially, severe difficulties appear in the energy equation. However, this difficulty due to the wide range in the ratio of variable to internal magnetic fields can be avoided from the fact that intrinsic magnetic field includes only potential components. Thus, it becomes important to construct the MHD calculations suppressing the direct inclusion of the intrinsic component of the magnetic field, as dependent variables [3] [19]. In this paper, therefore, a modified equation system is used to cope with such a problem, changing dependent variables.

In order to apply the MHD simulation to more complicated problems in space science, an additional improvements is imposed on the original MHD equations. Since space plasma does not always consist of single ion specie, sometimes we must treat the plasma that includes multi-component ions with the source and sink [9]. The ordinary 8-component MHD equations can be extended to the 9-component MHD equations for 2-component plasma.

It is shown in this paper that the equation system with the above modifications can still be written in the conservation form and can also be treated numerically through the FVM with the upwinding TVD flux. The eigenvalues and eigenvectors necessary to construct a TVD scheme are calculated for the 9-component MHD equations with modified variables. Construction of the scheme is seen in sections 2, 3, 4, and 5. In section 6, a brief comment is given about the suitability of the present scheme for parallel computation. To show the feasibility of the scheme, three numerical examples are shown in sections 7, 8, and 9. The first example in section 7 shows an excellent ability of present scheme for the capturing of shocks and discontinuities. The second example in section 8 demonstrates the applicability of the present scheme to multi-component plasma. The last example in section 9 adopts the present scheme to the space weather problem that includes a potential magnetic field, and shows the capability of low-noise calculation even in the low-β region.

2 TVD schemes for hyperbolic equations

The history of the development of numerical schemes for hyperbolic conservation law is long and rich [20]. The idea that stable computation can be accomplished through an approximate dissipation term was used in early schemes. The advection equation, the most simple hyperbolic equation, can be written in a one dimensional coordinate system $(x,\ t)$ as

$$\frac{\partial u}{\partial t} + C\frac{\partial u}{\partial x} = 0. \tag{1}$$

Where C is an advection speed. Let u_i^n be the numerical solution of (1) at $x = i\triangle x$ and $t = n\triangle t$. Then, the explicit time integration of this equation is

$$\frac{u_i^{n+1} - u_i^n}{\triangle t} = -C\frac{u_{i+1}^n - u_{i-1}^n}{2\triangle x} + \frac{d}{2}\frac{u_{i+1}^n - 2u_i^n + u_{i-1}^n}{\triangle t}. \tag{2}$$

The stability condition for equation (2) is $1 > d > k^2$, with $k = |C|\triangle t/\triangle x$. Friedrichs-Lax, Godunov, and Lax-Wendroff schemes are obtained automatically by selecting $d = 1, d = k = |C\triangle t/\triangle x|$, and $d = k^2 = (C\triangle t/\triangle x)^2$, respectively. Out of these schemes only the Lax-Wendroff scheme has the second order accuracy.

Modern shock-capturing schemes add only enough dissipation in small localized regions to eliminate numerical oscillations. These schemes enforce some constraint on the problem, usually that the solutions be TVD. The Godunov scheme can be modified to

$$u_i^{n+1} - u_i^n = C^-_{i+1/2}(u^n_{i+1} - u^n_i) - C^+_{i-1/2}(u^n_i - u^n_{i-1}), \tag{3}$$

with

$$C^-_{i+1/2} = (|C| - C)\triangle t/2\triangle x, C^+_{i-1/2} = (|C| + C)\triangle t/2\triangle x. \tag{4}$$

These coefficients satisfy the condition

$$0 < C^-_{i+1/2} + C^+_{i-1//2} < 1, 0 < C^-_{i+1/2}, C^+_{i-1//2}, \tag{5}$$

and the total variation at step $n+1$ under this condition is

$$\begin{aligned}
&TV(u^{n+1}) = \sum |u_{i+1} + C^-_{i+3/2}(u_{i+2} - u_{i+1}) - C^+_{i+1/2}(u_{i+1} - u_i) \\
&-u_{i+1} - C^-_{i+1/2}(u_{i+1} - u_i) + C^+_{i-1/2}(u_i - u_{i-1})| \\
&\leq \sum C^-_{i+3/2}|u_{i+2} - u_{i+1}| \\
&+ \sum (1 - C^+_{i+1/2} - C^-_{i+1/2})|u_{i+1} - u_i| \\
&+ \sum C^+_{i-1/2}|u_i - u_{i-1}| \\
&= \sum |u_{i+1} - u_i|.
\end{aligned} \tag{6}$$

Thus, the TVD is satisfied for the Godunov scheme. This sccheme is a first-order upwind TVD scheme.

In order to obtain a higher-order TVD scheme, we write equation (2) in the flux formula

$$\frac{u_i^{n+1} - u_i^n}{\triangle t} = -\frac{F^n_{i+1/2} - F^n_{i-1/2}}{\triangle x}, \tag{7}$$

then the Godunov and Lax-Wendroff fluxes in the case of $C > 0$ are

$$F^G_{i+1/2} = Cu_i, \tag{8}$$

and

$$F^L_{i+1/2} = Cu_i + C/2 \cdot (1 - k)(u_{i+1} - u_i), \tag{9}$$

respectively. Equation (8) shows the fact that the Godunov scheme is an upwind scheme. By combining Godunov and Lax-Wendroff fluxes as

$$F_{i+1/2} = (1 - B_{i+1/2})F^G_{i+1/2} + B_{i+1/2}F^L_{i+1/2}, \tag{10}$$

one can obtain

$$\frac{u_i^{n+1} - u_i^n}{u^n_{i-1} - u^n_i} = k - \frac{1}{2}k(1-k)B_{i-1/2} + \frac{1}{2}k(1-k)\frac{B_{i+1/2}}{r_i}, \tag{11}$$

with

$$r_i = (u_i - u_{i-1})/(u_{i+1} - u_i). \tag{12}$$

In order for the scheme to be TVD, the left hand side of equation (11) must be between 0 and 1 and the resulting sufficient condition obtained after some simple algebra is the following,

$$-\frac{2}{k} < -2 < B_{i-1/2} - \frac{B_{i+1/2}}{r_i} < 2 < \frac{2}{1-k}, \tag{13}$$

which reduces to

$$0 < B_{i+1/2}, B_{i+1/2}/r_i < 2. \tag{14}$$

Commonly used limiters which give the constraint for the TVD scheme satisfy this condition.

For a coupled nonlinear equation system

$$\frac{\partial \mathbf{u}}{\partial t} + \frac{\partial \mathbf{f}(\mathbf{u})}{\partial x} = 0, \mathbf{A} = \frac{\partial \mathbf{f}}{\partial \mathbf{u}}, \tag{15}$$

the Riemann problem is solved to evaluate the upwind flux. From the flux Jacobian matrix $\mathbf{A}$, its eigenvalues λ_k, and eigenvectors $\mathbf{r}_k$, $\mathbf{u}_{i+1} - \mathbf{u}_i$ can be expanded as

$$\mathbf{u}_{i+1} - \mathbf{u}_i = \sum C_k \mathbf{r}_k, C_k = \mathbf{r}_k^{-1} \triangle \mathbf{u}, \mathbf{A}_{i+1/2}\mathbf{r}_k = \lambda_k \mathbf{r}_k, \tag{16}$$

then, the upwind flux can be evaluated as

$$\begin{aligned}
&\mathbf{F}_{i+1/2} = \mathbf{f}(\mathbf{u}^R_{i+1/2}) = \mathbf{f}(\mathbf{u}_i + \sum\nolimits^- C_k \mathbf{r}_k) = \mathbf{f}(\mathbf{u}_i) + \mathbf{A}\sum\nolimits^- C_k \mathbf{r}_k \\
&= \mathbf{f}(\mathbf{u}_i) + \sum\nolimits^- \lambda_k C_k \mathbf{r}_k = \mathbf{f}_i/2 + (\mathbf{f}_{i+1} - \sum \lambda_k C_k \mathbf{r}_k)/2 + \sum\nolimits^- \lambda_k C_k \mathbf{r}_k \\
&= (\mathbf{f}_i + \mathbf{f}_{i+1})/2 - (\sum\nolimits^+ \lambda_k C_k \mathbf{r}_k - \sum\nolimits^- \lambda_k C_k \mathbf{r}_k)/2 \\
&= (\mathbf{f}_i + \mathbf{f}_{i+1})/2 - (\sum |\lambda_k| C_k \mathbf{r}_k)/2 \\
&= (\mathbf{f}_i + \mathbf{f}_{i+1})/2 - (\mathbf{R}|\mathbf{\Lambda}|\mathbf{R}^{-1}\triangle \mathbf{u})/2.
\end{aligned} \tag{17}$$

The accuracy of the scheme increases by considering the interpolationof dependent variables. An example is the MUSCL interpolation in which i and j are replaced by L and R as

$$\mathbf{u}_L = \mathbf{u}_i + \mathbf{s}_i\{(\mathbf{1} - \mathbf{s}_i/3)(\mathbf{u}_i - \mathbf{u}_{i-1}) + (\mathbf{1} + \mathbf{s}_i/3)(\mathbf{u}_{i+1} - \mathbf{u}_i)\}/4, \tag{18}$$

$$\mathbf{u}_R = \mathbf{u}_{i+1} - \mathbf{s}_{i+1}\{(\mathbf{1} + \mathbf{s}_{i+1}/3)(\mathbf{u}_{i+1} - \mathbf{u}_i) + (\mathbf{1} - \mathbf{s}_{i+1}/3)(\mathbf{u}_{i+2} - \mathbf{u}_{i+1})\}/4, \tag{19}$$

where $\mathbf{s}_i$ is a limiter at the grid point i.

Assuming first-order accuracy in implicit terms, we can also obtain an implicit MUSCL scheme as

$$\begin{aligned}
&\frac{\triangle x}{\triangle t}\triangle \mathbf{u}_i^{n+1} + \frac{\partial \mathbf{F}_{i+1/2}}{\partial \mathbf{u}_{i+1}}\triangle \mathbf{u}_{i+1}^{n+1} + \frac{\partial \mathbf{F}_{i+1/2}}{\partial \mathbf{u}_i}\triangle \mathbf{u}_i^{n+1} \\
&-\frac{\partial \mathbf{F}_{i-1/2}}{\partial \mathbf{u}_i}\triangle \mathbf{u}_i^{n+1} - \frac{\partial \mathbf{F}_{i-1/2}}{\partial \mathbf{u}_{i-1}}\triangle \mathbf{u}_{i-1}^{n+1} \\
&= -(\mathbf{F}^n_{i+1/2} - \mathbf{F}^n_{i-1/2}),
\end{aligned} \tag{20}$$

with a notation $\triangle \mathbf{u}_i^{n+1} = \mathbf{u}_i^{n+1} - \mathbf{u}_i^n$.

3 Finite volume TVD scheme for 9-component MHD equations

In space plasma simulation, sometimes we must treat multiple plasma components. The ideal MHD equations can be extended to the 9-component MHD equations that treat 2-component plasma. The nondimensional conservation-law form for these equations can be written in the Cartesian coordinate system (x,y,z,t) as

$$\frac{\partial \mathbf{u}}{\partial t}+\frac{\partial \mathbf{F}(\mathbf{u})}{\partial x}+\frac{\partial \mathbf{G}(\mathbf{u})}{\partial y}+\frac{\partial \mathbf{H}(\mathbf{u})}{\partial z}=\mathbf{S}, \tag{21}$$

where the dependent variables are $\mathbf{u}=(\rho,\mathbf{m},\mathbf{B},U,\rho_2)^T$ and $\mathbf{F},\mathbf{G},\mathbf{H}$, and $\mathbf{S}$ are flux functions in the x, y, z directions and source terms. $\rho,\mathbf{m},\mathbf{B}$ and U are the density, momentum, magnetic field and energy density. Where $\rho=\rho_1+\rho_2$ with ρ_1 and ρ_2 being the densities of first and second plasma components. Using Gauss's law, the integration form of equation (21) can be written as

$$\frac{\partial}{\partial t}\int \mathbf{u}dv+\int(\mathbf{F}n_x+\mathbf{G}n_y+\mathbf{H}n_z)ds=\int \mathbf{S}dv, \tag{22}$$

where dv and ds are the volume and surface element of the control volume and $\mathbf{n}$ is a unit vector normal to the surface of the control volume.

Let us define a matrix $\mathbf{T}$ which rotates the x axis to the direction of $\mathbf{n}$

$$\mathbf{T}=\begin{vmatrix} 1 & & & & \\ & \mathbf{T}_1 & & & \\ & & \mathbf{T}_1 & & \\ & & & 1 & \\ & & & & 1 \end{vmatrix}, \tag{23}$$

with

$$\mathbf{T}_1=\begin{vmatrix} n_x & n_y & n_z \\ t_{1x} & t_{1y} & t_{1z} \\ t_{2x} & t_{2y} & t_{2z} \end{vmatrix}, \tag{24}$$

then equation (22) is expressed as

$$\frac{\partial}{\partial t}\int \mathbf{u}dv+\int \mathbf{T}^{-1}\mathbf{T}(\mathbf{F}n_x+\mathbf{G}n_y+\mathbf{H}n_z)ds=\int \mathbf{S}dv, \tag{25}$$

where $\mathbf{t}_1$ and $\mathbf{t}_2$ are unit vectors tangent to the surface of the control volume and orthogonal to each other. Since the form of the MHD equations must be unchanged for the rotation of the coordinate system, the relation

$$\mathbf{T}(\mathbf{F}(\mathbf{u})n_x+\mathbf{G}(\mathbf{u})n_y+\mathbf{H}(\mathbf{u})n_z)=\mathbf{F}(\mathbf{T}\mathbf{u})=\mathbf{F}(\mathbf{u}_n) \tag{26}$$

must hold [15] [16] [19]. Then one can obtain from equation (25)

$$\frac{\partial}{\partial t}\int \mathbf{u}dv+\int \mathbf{T}^{-1}\mathbf{F}(\mathbf{u}_n)ds=\int \mathbf{S}dv. \tag{27}$$

Introducing new dependent variables $\mathbf{u}_1 = (\rho, \mathbf{m}, \mathbf{B}_1, U_1, \rho_2)^T = (\rho, m_x, m_y, m_z, B_x - B_{0x}, B_y - B_{0y}, B_z - B_{0z}, U - (\mathbf{B}_1 \cdot \mathbf{B}_0)/\beta - B_0^2/(2\beta), \rho_2)^T$, with the conditions $\partial \mathbf{B}_0/\partial t = rot\mathbf{B}_0 = div\mathbf{B}_0$, then the equation for $\mathbf{u}_1$ can be written in the conservaton-law form as

$$\frac{\partial}{\partial t}\int \mathbf{u}_1 dv + \int \mathbf{T}^{-1}\mathbf{F}(\mathbf{u}_{1n}, \mathbf{B}_{0n}) ds = \int \mathbf{S} dv, \qquad (28)$$

with $\mathbf{u}_{1n} = \mathbf{T}\mathbf{u}_1, \mathbf{m}_n = T_1\mathbf{m} = (m_n, m_{t1}, m_{t2})^T, \mathbf{B}_n = \mathbf{T}_1\mathbf{B} = (B_n, B_{t1}, B_{t2})^T$, $\mathbf{B}_{1n} = \mathbf{T}_1\mathbf{B}_1 = (B_{1n}, B_{1t1}, B_{1t2})^T$, and $\mathbf{B}_{0n} = \mathbf{T}_1\mathbf{B}_0 = (B_{0n}, B_{0t1}, B_{0t2})^T$. The flux function in the normalized form is written

$$\mathbf{F} = \begin{bmatrix} m_n \\ P + \frac{m_n m_n}{\rho} + \frac{B^2}{2\beta} - \frac{1}{\beta}B_n B_n - \frac{B_0^2}{2\beta} + \frac{1}{\beta}B_{0n}B_{0n} \\ \frac{m_{t1}m_n}{\rho} - \frac{1}{\beta}B_{t1}B_n + \frac{1}{\beta}B_{0t1}B_{0n} \\ \frac{m_{t2}m_n}{\rho} - \frac{1}{\beta}B_{t2}B_n + \frac{1}{\beta}B_{0t2}B_{0n} \\ 0 \\ \frac{m_n}{\rho}B_{t1} - \frac{m_{t1}}{\rho}B_n \\ \frac{m_n}{\rho}B_{t2} - \frac{m_{t2}}{\rho}B_n \\ \frac{m_n}{\rho}(U_1 + \frac{B_1^2}{2\beta} + P) - \frac{B_{1n}}{\beta} \\ \times(\frac{m_n}{\rho}B_{1n} + \frac{m_{t1}}{\rho}B_{1t1} + \frac{m_{t2}}{\rho}B_{1t2}) \\ +\frac{B_{1t1}}{\beta}(\frac{m_n}{\rho}B_{0t1} - \frac{m_{t1}}{\rho}B_{0n}) \\ +\frac{B_{1t2}}{\beta}(\frac{m_n}{\rho}B_{0t2} - \frac{m_{t2}}{\rho}B_{0n}) \\ \frac{\rho_2}{\rho}m_n \end{bmatrix}. \qquad (29)$$

In the solar wind-magnetosphere-ionosphere (S-M-I) interaction problem, a dipole field will be adopted as $\mathbf{B}_0$. In the expression of (29), the $\mathbf{B}_0$ terms are added to the second, third, fourth, and last components of F, considering $rot\mathbf{B}_0 \times \mathbf{B}_0 = 0$ and $\mathbf{m} \times \mathbf{B} \cdot rot\mathbf{B}_0 = 0$. The variable component of energy density U_1, density ρ, momentum $\mathbf{m}$, and the variable components of magnetic field $\mathbf{B}_1$ are related to pressure P by the equation

$$P = (\gamma - 1)(U_1 - \frac{m^2}{2\rho} - \frac{B_1^2}{2\beta}). \qquad (30)$$

Constants in these equations are β and γ, with $\beta = \mu\rho_0 RT_0/B_{00}^2, \gamma$ the polytropic index, μ the magnetic permeability, R the gas constant, ρ_0 the normalization density, B_{00} the normalization field, and T_0 the normalization temperature. Momentum $\mathbf{m}$ and time t are normalized by $\rho_0(RT_0)^{1/2}$ and $L_0/(RT_0)^{1/2}$, with L_0 normalization length.

From equation (28), a discrete formulation of the MHD equations in the FVM style is written for the grid point i in the form

$$\frac{\partial}{\partial t}\mathbf{u}_{1i}V_i + \sum\nolimits_j \mathbf{T}_{ij}^{-1}\underline{\mathbf{F}}_{ij}(\mathbf{u}_{1ni'}, \mathbf{u}_{1ni}, \mathbf{u}_{inj}, \mathbf{u}_{1nj'}, \mathbf{B}_{0nij})S_{ij} = \mathbf{S}V_i, \qquad (31)$$

where j denotes the grid points neighboring the grid point i, V_i denotes the volume of the control volume cell which includes the grid point i, $\mathbf{T}_{ij}$ is the rotation matrix at the interfacing surface between i and j, S_{ij} is the surface area of the i and j interface, $\mathbf{u}_{1ni'}, \mathbf{u}_{1ni}, \mathbf{u}_{1nj}$, and $\mathbf{u}_{1nj'}$ are $\mathbf{u}_{1i'}, \mathbf{u}_{1i}, \mathbf{u}_{1j}$, and $\mathbf{u}_{1j'}$ rotated by $\mathbf{T}_{ij}$, and $\mathbf{B}_{0nij}$ is $\mathbf{B}_{0n}$ at the i and j interface. Adopting equation (17), the first-order upwind numerical flux $\underline{\mathbf{F}}_{ij}$ for equation (31) is given as

$$\underline{\mathbf{F}}_{ij} = \frac{1}{2}[\mathbf{F}(\mathbf{u}_{1nj}, \mathbf{B}_{0nij}) + \mathbf{F}(\mathbf{u}_{1ni}, \mathbf{B}_{0nij}) - \mathbf{R}_{ij} \mid \mathbf{\Lambda}_{ij} \mid \mathbf{R}_{ij}^{-1}(\mathbf{u}_{1nj} - \mathbf{u}_{1ni})]. \quad (32)$$

Here, the mode synthesis matrix $\mathbf{R}_{ij}$ and the eigenvalue matrix $\mathbf{\Lambda}_{ij}$ are calculated from the following diagonalization process:

$$\mathbf{A}_{ij}\mathbf{R}_{ij} = \mathbf{R}_{ij}\mathbf{\Lambda}_{ij}, \quad (33)$$

$$\mathbf{A}_{ij} = \frac{\partial \mathbf{F}}{\partial \mathbf{u}_{1n}}(\mathbf{u}_{inij}, \mathbf{B}_{0nij}), \quad (34)$$

with $\mathbf{A}_{ij}$ the flux Jacobian matrix of $\mathbf{F}$ at the i and j interface, and $\mathbf{u}_{1nij}$ a symmetric average of $\mathbf{u}_{1nj}$ and $\mathbf{u}_{1ni}$. As seen from equation (33), the mode synthesis matrix consists of the right eigenvectors of the flux Jacobian matrix $\mathbf{r}_{ijk}$, and the diagonal matrix $\mathbf{\Lambda}_{ij}$ consists of eigenvalues $\lambda_{ijk}, k = 1{\sim}9$.

To get a higher order of accuracy, the MUSCL approach is used changing i and j in equation (32) to L and R, suffixes which indicate variables just on the negative and positive sides of the interface [17]. Adopting equations (18) and (19), then the numerical flux is defined by the following relation:

$$\underline{\mathbf{F}}_{ij} = \frac{1}{2}[\mathbf{F}(\mathbf{u}_{1nR}, \mathbf{B}_{0nij}) + \mathbf{F}(\mathbf{u}_{1nL}, \mathbf{B}_{0nij}) - \mathbf{R}_{RL} \mid \mathbf{\Lambda}_{RL} \mid \mathbf{R}_{RL}^{-1}(\mathbf{u}_{1nR} - \mathbf{u}_{1nL})], \quad (35)$$

with

$$\mathbf{A}_{RL}\mathbf{R}_{RL} = \mathbf{R}_{RL}\mathbf{\Lambda}_{RL}, \quad (36)$$

$$\mathbf{u}_{1nL} = \mathbf{u}_{1ni} + \mathbf{s}_i(\mathbf{1} - \mathbf{s}_i/3)(\mathbf{u}_{1ni} - \mathbf{u}_{1ni'}) + (\mathbf{1} + \mathbf{s}_i/3)(\mathbf{u}_{1nj} - \mathbf{u}_{1ni})/4, \quad (37)$$

$$\mathbf{u}_{1nR} = \mathbf{u}_{1nj} - \mathbf{s}_j(\mathbf{1} - \mathbf{s}_j/3)(\mathbf{u}_{1nj'} - \mathbf{u}_{1nj}) + (\mathbf{1} + \mathbf{s}_j/3)(\mathbf{u}_{1nj} - \mathbf{u}_{1ni})/4, \quad (38)$$

where the diagonal matrices $\mathbf{s}_i$ and $\mathbf{s}_j$ consist of the so-called Van Leer's differentiable limiter. The k-th components of s_i and s_j are calculated from the k-th components of $\mathbf{u}_{1n}$. Without the suffixes 1 and k, they are written as

$$s_i = \frac{2(u_{nj} - u_{ni})(u_{ni} - u_{ni'}) + \epsilon}{(u_{nj} - u_{ni})^2 + (u_{ni} - u_{ni'})^2 + \epsilon}, \quad (39)$$

$$s_j = \frac{2(u_{nj'} - u_{nj})(u_{nj} - u_{ni}) + \epsilon}{(u_{nj'} - u_{nj})^2 + (u_{nj} - u_{ni})^2 + \epsilon}, \quad (40)$$

with ϵ a small number. Interpolation points i ' and j ' are obtained by extending the line which connects grid points i and j to the neighboring surface of control volumes.

A serious problem in numerical MHD simulations involves the violation of the $div\mathbf{B} = 0$ condition. Not only numerical roundoff errors but also the use of upwind fluxes and a non-Cartesian grid system make it difficult to fulfill the

$div\mathbf{B} = 0$ condition automatically. In the present calculation, an extra equation is added to eliminate artificial magnetic monopoles [21]. The variable components of magnetic field $\mathbf{B}_1$ are replaced every several time steps, by a new field $\mathbf{B}_{1c}$ given as

$$\mathbf{B}_{1c} = \mathbf{B}_1 + grad\phi, \tag{41}$$

$$\bigtriangledown^2\phi = -div\mathbf{B}_1. \tag{42}$$

To solve equation (41), the conjugate residual (CR) method is applied.

4 Eigenvalues and eigenvectors for the 9-component MHD equations

In this section, eigenvalues and eigenvectors are shown for the 9-component MHD equations. For the Jacobian matrix of flux fuction (29), eigenvalues $\lambda_k, k = 1{\sim}9$ are [14]

$$\lambda_1 = m'_n, \tag{43}$$

$$\lambda_{2,3} = m'_n \pm |B'_n|, \tag{44}$$

$$\lambda_{4,5} = m'_n \pm V_f, \tag{45}$$

$$\lambda_{6,7} = m'_n \pm V_s, \tag{46}$$

$$\lambda_8 = 0, \tag{47}$$

$$\lambda_9 = m'_n, \tag{48}$$

where

$$V_f^2, V_s^2 = \frac{1}{2}[C_0 + B'^2 \pm \{(C_0 + B'^2)^2 - 4C_0 {B'_n}^2\}^{1/2}], \tag{49}$$

$$C_0 = \gamma P/\rho, \tag{50}$$

with the notation $\mathbf{u}'_n = (\rho, \mathbf{m}'_n, \mathbf{B}'_n, U, \rho_2)^T = (\rho, m_n/\rho, m_{t1}/\rho, m_{t2}/\rho, B_n/\sqrt{\beta\rho}, B_{t1}/\sqrt{\beta\rho}, B_{t2}/\sqrt{\beta\rho}, U, \rho_2)^T$. In the expresion of eigenvalues,$\sqrt{C_0}, |B'_n|, V_f$ and V_s correspond to sound, Alfen, fast and slow velocities, respectively. In addition to one entropy, two Alfven, two fast and two slow waves of normal MHD equations, there appears one more entropy wave in the 9-component MHD equations. Calculations of eigenvectors must be done with special care avoiding the degeneration of eigenvectors when wave propagations become perpendicular or parallel to the magnetic field. The right eigenvectors $\mathbf{r}_k$ which correspond to λ_k are [19]

$$\mathbf{r}_1 = \begin{bmatrix} 1 \\ m'_n \\ m'_{t1} \\ m'_{t2} \\ 0 \\ 0 \\ 0 \\ 0.5{\cdot}m'^2 \\ 0 \end{bmatrix}, \tag{51}$$

$$\mathbf{r}_{2,3} = \begin{bmatrix} 0 \\ 0 \\ \mp B''_{t2}{\cdot}sgn(B'_n) \\ \pm B''_{t1}{\cdot}sgn(B_n) \\ 0 \\ B''_{t2}\sqrt{\frac{\beta}{\rho}} \\ -B''_{t1}\sqrt{\frac{\beta}{\rho}} \\ \mp(B''_{t2}m'_{t1} - B''_{t1}m'_{t2}){\cdot}sgn(B'_n) + (B''_{t2}B'_{1\,t1} - B''_{t1}B'_{1\,t2}) \\ 0 \end{bmatrix}, \tag{52}$$

$$\mathbf{r}_{4,5} = \begin{bmatrix} a_f \\ a_f(m'_n \pm V_f) \\ a_f m'_{t1} \mp a_s B''_{t1} V_f B'_n \\ a_f m'_{t2} \mp a_s B''_{t2} V_f B'_n \\ 0 \\ a_s B''_{t1} V_f^2 \sqrt{\frac{\beta}{\rho}} \\ a_s B''_{t2} V_f^2 \sqrt{\frac{\beta}{\rho}} \\ a_f{\cdot}0.5{\cdot}m'^2 + a_f V_f^2/(\gamma-1) \pm a_f V_f m'_n \\ \mp a_s V_f (B''_{t1}m'_{t1} + B''_{t2}m'_{t2}) B'_n \\ + a_f(-1)/(\gamma-1)(V_f^2 - C_0) \\ + a_f(V_f^2 - C_0)(B''_{t1}B''_{1\,t1} + B''_{t2}B''_{1\,t2}) \\ /({B''_{t1}}^2 + {B''_{t2}}^2) \\ a_f\rho_2/\rho \end{bmatrix}, \tag{53}$$

$$\mathbf{r}_{6,7} = \begin{bmatrix} a_s \\ a_s(m'_n \pm V_s) \\ a_s m'_{t1} \pm a_f B''_{t1}\sqrt{C_0}/V_f{\cdot}sgn(B'_n) \\ a_s m'_{t2} \pm a_f B''_{t2}\sqrt{C_0}/V_f{\cdot}sgn(B'_n) \\ 0 \\ -a_f B''_{t1}\sqrt{\frac{\beta}{\rho}}C_0/V_f^2 \\ -a_f B''_{t2}\sqrt{\frac{\beta}{\rho}}C_0/V_f^2 \\ a_s{\cdot}0.5{\cdot}m'^2 + a_s V_s^2/(\gamma-1) \pm a_s V_s m'_n \\ \pm a_f(B''_{t1}m'_{t1} + B''_{t2}m'_{t2}) \\ \times\sqrt{C_0}/V_f{\cdot}sgn(B'_n) + a_s(-1)/(\gamma-1)(V_s^2 - C_0) \\ + a_s(V_s^2 - C_0)(B''_{t1}B''_{1\,t1} + B''_{t2}B''_{1\,t2}) \\ /({B''_{t1}}^2 + {B''_{t2}}^2) \\ a_s\rho_2/\rho \end{bmatrix}, \tag{54}$$

$$\mathbf{r}_8 = \begin{bmatrix} 0 \\ 0 \\ 0 \\ 0 \\ 1 \\ 0 \\ 0 \\ 0 \\ 0 \end{bmatrix}, \tag{55}$$

$$\mathbf{r}_9 = \begin{bmatrix} 1 \\ m'_n \\ m'_{t1} \\ m'_{t2} \\ 0 \\ 0 \\ 0 \\ 0.5{\cdot}m'^2 \\ 1 \end{bmatrix}, \tag{56}$$

where

$$B''_{t1} = (B'_{t1} + \epsilon)/(B'^2_{t1} + B'^2_{t2} + 2\epsilon^2)^{1/2}, \tag{57}$$

$$B''_{t2} = (B'_{t2} + \epsilon)/(B'^2_{t1} + B'^2_{t2} + 2\epsilon^2)^{1/2}, \tag{58}$$

$$B_1{}''_{t1} = (B_1{}'_{t1} + \epsilon)/(B'^2_{t1} + B'^2_{t2} + 2\epsilon^2)^{1/2}, \tag{59}$$

$$B_1{}''_{t2} = (B_1{}'_{t2} + \epsilon)/(B'^2_{t1} + B'^2_{t2} + 2\epsilon^2)^{1/2}, \tag{60}$$

$$a_f = (V_f^2 - B'^2_n)^{1/2}/(V_f^2 - V_s^2)^{1/2}, \tag{61}$$

$$a_s = (V_f^2 - C_0)^{1/2}/(V_f^2 - V_s^2)^{1/2} V_f, \tag{62}$$

and ϵ is a small number.

5 Source terms and boundary conditions

The selection of source terms and boundary conditions depends on the kind of problem treated by the MHD simulation. Typical source terms considered in space science are ion production and loss, gravitational acceleration and aeronomic friction. They are written as

$$\mathbf{F} = \begin{vmatrix} q_1 + q_2 - L_1 - L_2 \\ -\nu\mathbf{m} - \rho\mathbf{g} \\ \mathbf{0} \\ -\mathbf{m}/\rho{\cdot}(\nu\mathbf{m} + \rho\mathbf{g}) + T_q(q_1 + q_2)/(\gamma - 1) - T_L(L_1 + L_2)/(\gamma - 1) \\ q_2 - L_2 \end{vmatrix}, \tag{63}$$

where q_i and L_i ($i = 1, 2$) are ion production and loss terms for i-th ion species, T_q is the temperature of ions when they are produced, T_L is the temperature of ions when they are lost. ν and $\mathbf{g}$ are ion-neutral collision frequency and gravitational acceleration. Production and loss rates q_i and L_i $(i = 1, 2)$ are normalized by ρ_0 and $L_0/(RT_0)^{1/2}$.

A typical boundary condition on the outer boundary is to give a plasma flow on the upstream side and a zero gradient condition on the downstream side. Commonly used boundary conditions on the inner boundary are ion chemical equilibrium, given plasma velocity, or zero gradient condition. In the case of S-M-I coupling, the plasma velocity perpendicular to the ambient magnetic field is decided from the field aligned current (FAC) flowing into the ionosphere. Assuming a spherical ionosphere at r=1 R_e, these processes are simulated on the inner boundary and on the ionosphere from

$$\nabla\cdot\sigma\nabla\phi_I = G_m(rot\mathbf{B}_1\cdot\mathbf{n}_b) = J_{\|}, \tag{64}$$

$$\sigma = \sigma_{EUV} + \sigma_{Diff}(P, \rho) + \sigma_J(J_{\|}), \tag{65}$$

$$\phi_m = \phi_I - f_1(J_{\|})|J_{\|}|, \tag{66}$$

$$\mathbf{m} - (\mathbf{m}\cdot\mathbf{n}_b)\mathbf{n}_b = -\rho\nabla\phi_m\times\mathbf{B}/B^2, \tag{67}$$

where σ is the ionospheric conductivity tenser, ϕ_I is the ionospheric potential, ϕ_m is the magnetospheric potential, $J_{\|}$ is the FAC, $\mathbf{n}_b$ is a unit vector along $\mathbf{B}$, and G_m is a geometrical factor associated with the mapping along field lines from r=3 R_e to r=1 R_e. σ_{EUV}, σ_{Diff}, and σ_J are the ionospheric conductivities due to the solar EUV, the diffuse auroral precipitation modeled by the pressure and temperature, and discreet precipitation modeled by the upward FAC [5]. Parallel potential is introduced through f_1 that is constant at the upward FAC and 0 at the downward FAC.

6 Parallel computation in a spherical geometry

Recently, the most powerful super-computers, such as the Fujitsu VPP and NEC SX, adopt the vector-parallel architecture with a distributed memory system. Efficient utilization of these vector-parallel super-computers is essential for the future study of space MHD simulations. In parallel computations with a distributed memory system, it is desirable to set a one-dimensional structuring axis in the three-dimensional space. In a spherical geometry that is important for space science, this "parallel" axis is chosen to be the radial direction. An unstructured grid can then be generated on spherical surfaces which construct the remaining two-dimensional space.

In the construction process of the grid system, it is desirable that two-dimensional spherical surfaces are covered by control volumes of similar size, because the integration time step is restricted by the smallest control volume. An example for such kind of grid system is shown in Fig. 1. The left panel in Fig. 1 shows the grid structure on the spherical inner boundary, while the right panel shows how to construct a 3-D grid structure by extending the position of spherically allocated grids outward from the inner boundary.

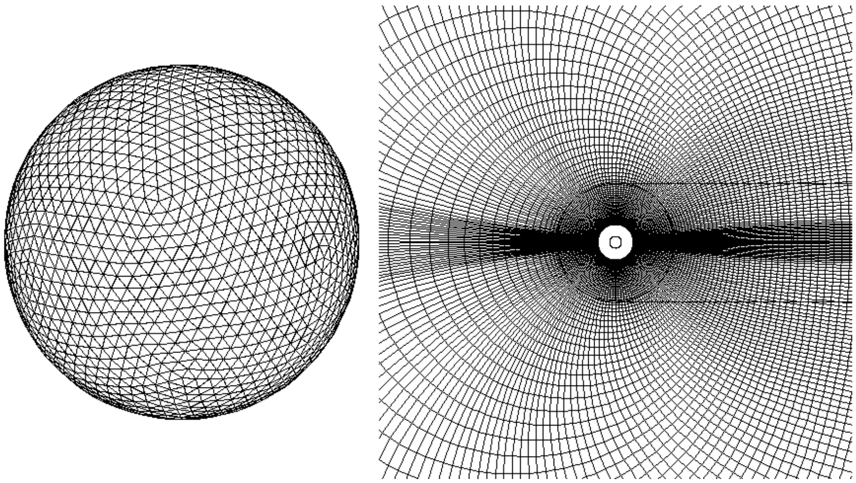

Fig. 1. Grid structure for the 3-D FVM calculation

In parallel computations on the distributed memory system of vector-parallel computers, it is important to identify the difference between distributed and redundant data areas. The parallel axis is used to distribute dependent variables to processors and to define the overlap data areas. In the finite volume TVD scheme, the most serious load in calculations comes from those for eigenvalues (43-50), eigenvectors (51-62), limiters (39,40) and numerical flux (29). These calculations are done sequentially in subroutines on a two-dimensional redundant data area, after copying 3-D dependent variables from a distributed data area to two-dimensionl redundant data areas. Using this method means that we do not have to rewrite subroutines with parallel programming constructs. The parallelization then occurs only in the main program which calls these subroutines. In the calculation of numerical flux, the dependent variables on the neighboring grid point of the calculation point must be referred to. To enable this referring in the parallel computation, the overlap data areas are used with the data transmission. Overlap data must be synchronized to data in the neighboring processors before the subroutines begin concurrent operation. After the main calculations, the final correction of the dependent variables is done in the main program, on the distributed data area. Finally, two processors calculate the inner and outer boundary conditions.

7 Numerical example 1 (Heliospheric structure)

The pressure difference between the solar corona and interstellar space drives the ionized solar atmosphere outward, despite the restraining influence of solar gravity. The solar wind thus generated interacts with the very local interstellar medium (VLISM) at some large distance from the sun. Here, the volume of the space created by the solar wind is called the heliosphere [8] [10] [11] [22] [23]. In this section, results are shown for the MHD simulation of the heliosphere.

At a distance where the local ram pressure of the solar wind becomes comparable to the external VLISM pressure, the solar wind shocks to form the termination shock (TS), which is a strong shock with a compression ratio 4. Then outside the TS, the shocked subsonic solar wind flows to the downstream direction of a uniform interstellar flow surrounding the heliosphere. This region constrained by the VLISM and filled with shocked solar wind plasma is called as heliosheath (HS). It is bounded inside by the TS and outside by a tangential discontinuity between the heliosphere and the VLISM called the heliopause (HP). Some observational evidences suggests that the interstellar wind is also supersonic. The supersonic interstellar flow recognizes the shocked solar wind plasma in the HS as an obstacle and forms a bow shock (BS), which is a magnetoacoustic shock. The shocked interstellar wind inside the BS contacts the shocked solar wind through the HP.

Since the formation process of the heliosphere generates many shocks and discontinuities, it offers a good problem to test the shock-capturing capability of the TVD scheme. The outer and inner boundaries for the calculation are set at 1000 AU and 50 AU. In this section, the interstellar plasma and the solar wind plasma are assigned to ρ_1 and ρ_2, respectively. Consequently, ρ_1 is zero at the inner boundary and ρ_2 is zero at the upstream boundary. On the inner boundary, a supersonic solar wind is adopted. The solar wind speed and density at 1 AU are assumed to be 400 km/sec and 5 cm^{-3} respectively, and the strength of the toroidal interplanetary magnetic field (IMF) here is assumed to be 2.8*cos(θ) nT with θ the heliolatitude. Toward the outer boundary, the solar wind maintains a constant velocity while its density and magnetic field fall with heliocentric distance r as r^{-2} and r^{-1}. The solar wind temperature at the inner boundary is assumed to be 10^4 K. The speed, density and temperature of the interstellar medium are assumed to be 25 km/sec, 0.1 cm^{-3}, and 10^4 K. The direction of the interstellar flow and magnetic field are assumed to be parallel to the ecliptic plane (toward -x) and to the solar rotational axis (toward $+z$). The strength of interstellar magnetic field is 0.15 nT. $\mathbf{S}$ and $\mathbf{B}_0$ are not considered in this problem.

Figure 2 shows the normalized equipressure (P) contour on the polar (upper half) and ecliptic (lower half) planes. The interstellar wind is from the right. The normalization value for P and contour spacing are 0.0144 pPa and 0.7, respectively. From the pressure distribution, the major structures of the heliosphere, the TS with Mach disk, the HP, and the BS are clearly visible as discontinuities. These high-quality resolutions of discontinuities are due to the excellent shock-capturing property of the TVD scheme.

At the BS the kinetic energy of the interstellar wind is converted to thermal and magnetic energies. Downstream of the BS, consequently, gas pressure dominates over the kinetic pressure. At the HP, increased gas and magnetic pressure are supported by the HS plasma pressure which is maintained by a supply of shocked solar wind pressure from the TS. The highest pressure in the HS appears

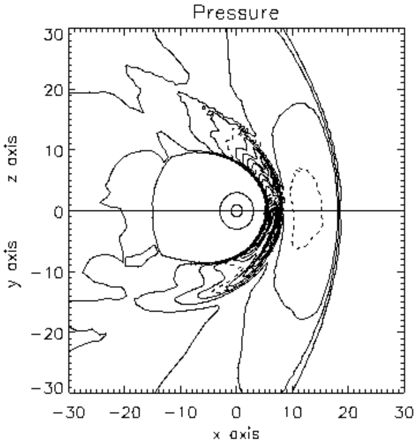

Fig. 2. Pressure distribution in the heliosphere

in the nose region because it must finally balance with the dynamic pressure of the interstellar wind.

The enhanced HS pressure around the nose region accelerates the shocked solar wind plasma toward the heliotail (HT). At the flank of the heliosphere, the oblique TS also helps the HS flow direct downtail based on the principle that at an oblique shock the downstream flow is always deflected away from the shock normal. On the contrary, the tailside TS consists of right-angle shock, because the post-shock flow can direct downtail as it is. Consequently, tangential discontinuity develops in the downstream HT, to separate fast HT flow that continues from the flank HS from a slow HT flow that exits directly from the tailside TS. This is a basic mechanism to form a bullet-shaped TS (Mach disk) on the downstream side [11].

8 Numerical example 2 (Solar wind-Venus interaction)

Since the internal magnetic field of Venus is negligibly small, the solar wind makes a direct contact with the ionosphere. When the interaction processes between the solar wind and planetary ionospheres are studied, at least two plasma components must be considered [9] [24] [25]. In the case of venusian ionosphere, the primary component of ionospheric plasma is O^+ ions, whereas the primary component of the solar wind is H^+ ions. So one must consider two plasma components to distinguish the ionospheric plasma from the solar wind plasma. In this section, therefore, the solar wind plasma and ionospheric plasma are assigned to ρ_1 and ρ_2, respectively. In this problem, source terms $\mathbf{S}$ are essentially important, because the high-density low-temperature ionospheric plasma that supports the impinging solar wind stratifies gravitationally on the balance of ion production and loss, neutral drag, and the gravitational acceleration. For the calculation of ρ_2, L_2, and ν, a stratified atmosphere composed of O and CO_2 is assumed around the planet. q_1, L_1, and $\mathbf{B}_0$ are set to zero in this section.

The inner and outer boundaries of the calculation region are at 1 R_p and 10 R_p, with R_p the planetary radius. On the outer boundary, the solar wind flow is given on the upstream ($+x$) side while the zero gradient condition is adopted on the downstream ($-x$) side. Where the IMF is assumed to be parallel to the y-axis. Near the inner boundary, the ion-neutral collision and ion chemical processes become dominant. Therefore, the ion chemical equilibrium and zero plasma velocity conditions are adopted on the inner boundary. Since the scale sizes of the ionosphere and the solar wind are quite different from each other, the grid points must be allocated so as to be dense in the ionosphere and coarse in the solar wind.

Figure 3 shows the result for the distributions of O^+ (left) and total ($=H^+ + O^+$, right) ion densities. The solar wind is from the left. The left and right panels in Fig. 3 show contours of $\log(\rho_2/\rho_{sw})$ and $\log(\rho/\rho_{sw})$, respectively. Where ρ_{sw} is the solar wind density. The contour spacing is 0.2 and the dashed contours are used at every 1.0. The minimum contour value for a dashed contour is 0.0. The upper and lower halves of the two panels show sun-planet meridian planes and equatorial planes defined by the direction of the IMF. The solid circles show the size of the planet. An excellent capturing of shocks and discontinuities is seen in Fig. 3. Results of the calculation show the formation of the BS, magnetic barrier and the ionopause in the dayside region. At the ionopause, the primary ion species change from H^+ on the high-altitude side to O^+ on the low-altitude side. In the nightside region, the ionospheric structure shows rather complex features. A part of O^+ ions penetrates into the magnetotail which results from the draping process of the IMF. Then, the penetrating O^+ ions tend to gather toward the central part of the magnetotail and form a high-density region. In

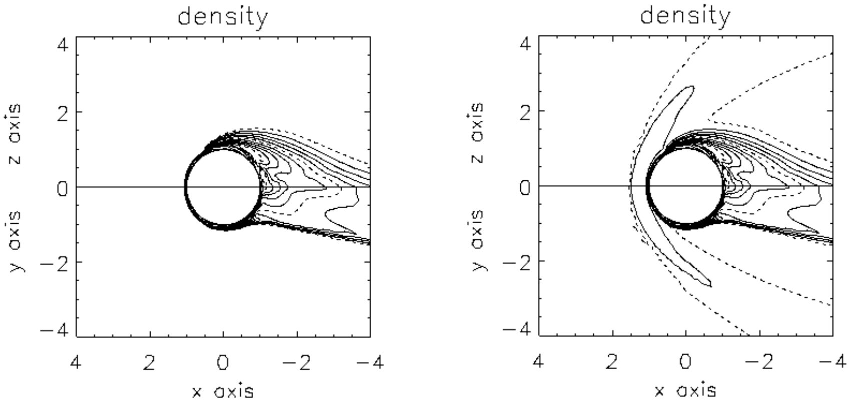

Fig. 3. O^+ density (left) and H^++O^+ density (right) around the planet

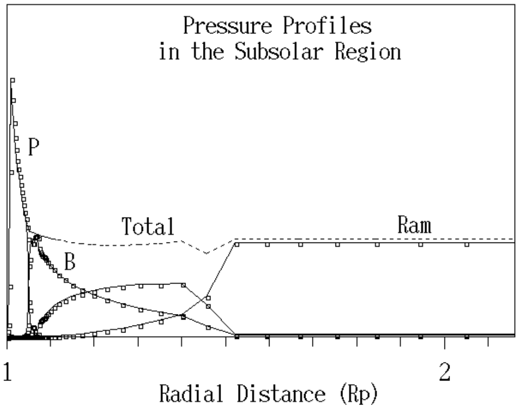

Fig. 4. Pressure balance along the sun-planet line

these results, the solar wind and ionospheric plasmas are distinguished clearly by the 9-component MHD equations.

Figure 4 shows altitude distributions of fluid pressure (P), magnetic pressure (B) and plasma dynamic pressure (Ram) at the subsolar point. Where small rectangles show positions of radial grid points. The pressures are normalized by the solar wind pressure. In the upstream solar wind, plasma kinetic energy dominates both of fluid pressure and magnetic pressure. At the BS, plasma kinetic energy is converted to plasma thermal energy. As a result, the fluid pressure becomes dominant after passing the BS. Approaching the ionopause, the magnetic pressure increases while the plasma pressure decreases, due to the formation of the magnetic barrier. At the ionopause, the magnetic barrier is supported by the fluid pressure of cold ionospheric plasma. This pressure of cold ionospheric plasma is maintained by the photoionization and ion chemical processes in the planetary upper atmosphere. The plasma pressure on the bottom side of the ionosphere is supported by the neutral atmosphere through ion-neutral collisions.

9 Numerical example 3 (Substorm and space weather)

A goal of the space weather effort is to increase our understanding of the S-M-I coupling system. In recent years, the global MHD simulation has become increasingly successful at constructing and predicting the behavior of the S-M-I system [1] [5] [6] [12]. It gives a theoretical foundation for the complex behavior of the S-M-I system that is controlled by the coupling process between different regions.

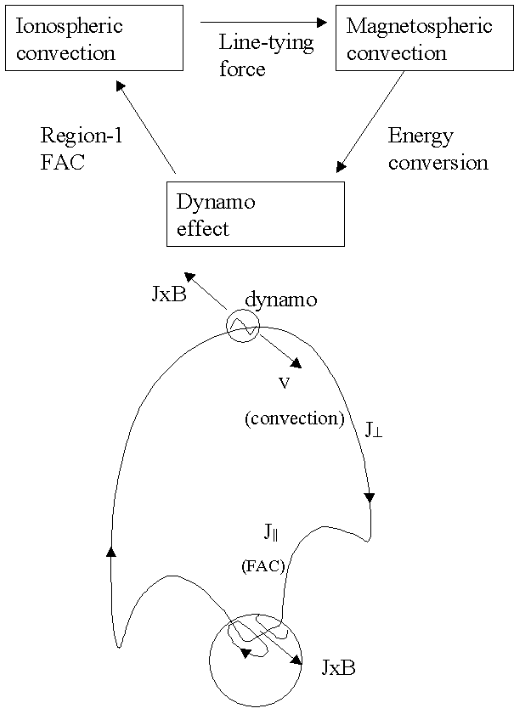

Fig. 5. Magnetospheric convection

In the solar wind interaction with the magnetosphere, energy and momentum are transferred from the solar wind to the magnetosphere through non-ideal MHD processes, to generate magnetospheric plasma convection [4]. Figure 5 schematically shows the construction of convection system. In the magnetosphere, the large-scale transportation of plasma is equivalent to a global electric field. The process driving the magnetospheric convection is at the same time the process generating the FACs, because the magnetospheric perpendicular stress must be transmitted to the polar ionosphere so as the ionospheric convection to follow the magnetospheric convection [3] [26]. In the current circuit connecting the magnetospheric dynamo and the conducting ionosphere, the $\mathbf{J}\times\mathbf{B}$ force in the ionosphere acts to accelerate the ionospheric convection against atmospheric friction. As a counter part of this energy dissipation in the ionosphere, FACs must be powered through the dynamo driven by the energy conversion in the convection system. Therefore, acting as a load for the magnetospheric convection in the M-I coupling system, the ionosphere controls the intensity of FAC.

In this section, we investigate the M-I processes that maintain the self-consistency in the convection system, including the generation mechanism of the M-I current systems, the ionospheric control of the magnetospheric configuration, and possible extension of convection status to the substorm. The FAC and plasma convection play a central role in the M-I coupling, while the state of energy source for these current systems depends on the solar wind-magnetospheric interaction. To improve our understanding of this problem, therefore, a self-consistent treatment is required for the coupling effects between three different regions, namely the solar wind, the magnetosphere and the ionosphere.

In the numerical study of the S-M-I coupling process, numerical errors in the low-β region near the ionosphere should be reduced. For this purpose, the MHD calculation is reconstructed as shown in equation (29) to suppress the direct inclusion of the potential component of the magnetic field as dependent variables. From these situations, a dipole magnetic field is assumed as $\mathbf{B}_0$. $\mathbf{S}$ and ρ_2 are not considered in this section. The outer and inner boundaries for the simulation are at 200 R_e and 3 R_e. A uniform solar wind with a speed of 350 km/sec and an IMF magnitude of 5 nT is assumed at the upstream boundary and zero gradients are assumed at the downstream boundary. Dependent variables are projected along the field line from the inner boundary (=3.0 R_e) to the ionosphere. In the ionosphere, equations (64) and (65) are solved to match the divergence of the Pedersen and Hall currents with the FAC.

Figure 6 shows the response of the magnetosphere to the southward turning of the IMF. The color figure shows the pressure distribution in the noon-midnight meridian plane of the magnetosphere at three times. Where P is normalized by the solar wind P. The bottom row illustrates the initial magnetospheric configuration for the northward IMF. At this time (7.7 minutes after the southward turning of the IMF), a thick and low-pressure plasma sheet is observed. The flow structure at this time (not shown) indicates that x line is situated beyond x=-60 R_e, which is the remnant of merging cell structure under the northward IMF condition [4] and called the distant neutral line. The growth phase shown in the second row (59 minutes after the southward turning of the IMF) is characterized by erosion of the dayside magnetosphere, thinning of the plasma sheet, and an increase in the flaring angle. The tail-like configuration of the plasma sheet during the growth phase is the consequence of an enhanced convection.

The substorm onset occurs as an abrupt change of the magnetospheric configuration in the near-earth tail. The top row in Fig. 6 (72.6 minutes after the southward turning of the IMF) shows the pressure distribution after the onset illustrating the appearance of the high-pressure region in the inner magnetosphere and the formation of the NENL in the midtail. Figure 6 also shows pressure and V_x distributions along the -x axis in the near-earth and midtail regions before and after the onset. Where V_x is normalized by the solar-wind sound velocity. After t=70 min, a sudden change of pressure profile is seen to start just like a transition from one state to another [5]. Before the onset (t<70 min), the strongest $-\nabla P$ force acts in the region between x=-10 and -20 R_e. As a result, earthward convection is obstructed at x=-14 R_e. In addition, a gradual formation of NENL is seen at x=-33 R_e before the onset. After the onset (t>70 min), the peak position in the pressure distribution shows a rapid inward movement. The pressure peek abruptly moves further inward to x=-8 R_e. At the same time, the convection flow intrudes into the inner magnetosphere inside x=-10 R_e in-

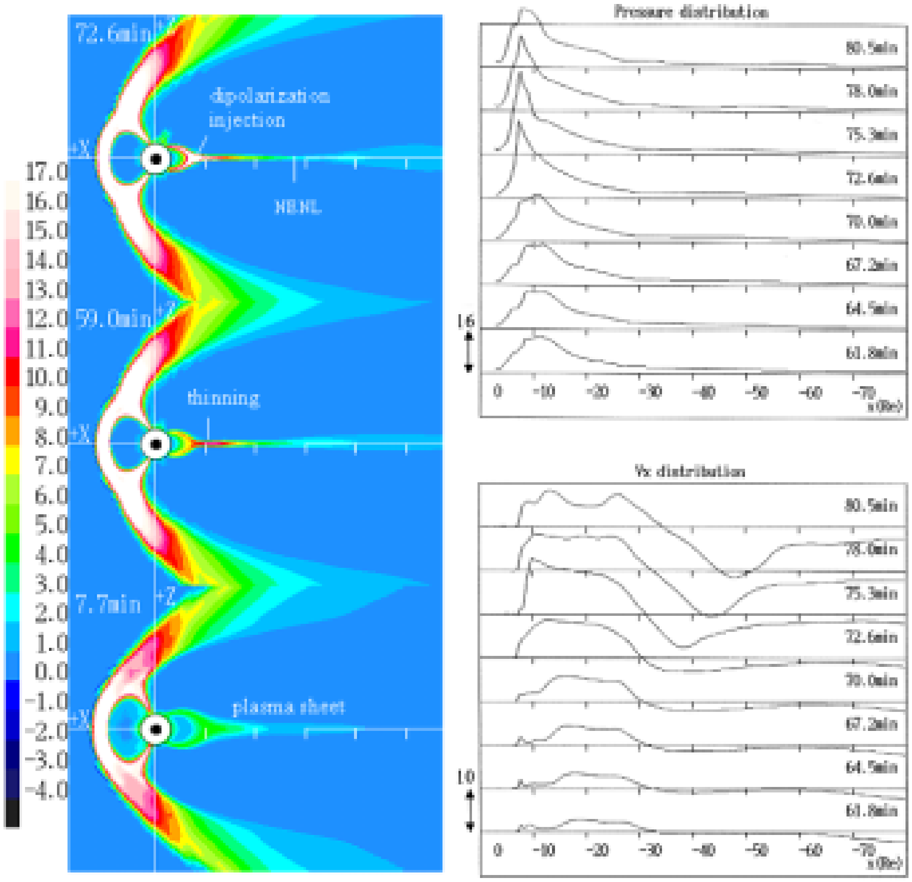

Fig. 6. Substorm sequence obtained from the MHD simulation

creasing in magnitude. Through these transition processes, a new stress balance is achieved in the near-earth plasma sheet in which recovered magnetic tension is balanced by newly established pressure inside x=-10 R_e. This pressure change is, in turn, a result of energy conversion from magnetic energy to internal energy caused by the pumping effect of convection associated with the recovery of magnetic tension. The fastest earthward flow in the plasma sheet appears after about 5 minutes from the onset. Then, tailward flow increases its speed. After t=75.3 min, the NENL begins to gradually retreat downtail.

During substorms, the ionospheric conductance enhances to a large extent due to precipitating particles which carry enhanced FACs. As a result, the coupling rate between the magnetosphere and the ionosphere becomes stronger, and the magnetosphere comes to hold a heavier load. However, the role of a variable M-I coupling in substorm onset is not clear at the present time [5].

References

1. T. Ogino: J. Geophys. Res. **91**, 6791 (1986)
2. T. Tanaka: J. Geophys. Res. **98**, 17,251 (1993)
3. T. Tanaka: J. Geophys. Res. **100**, 12,057 (1995)
4. T. Tanaka: J. Geophys. Res. **104**, 14,683 (1999)
5. T. Tanaka: J. Geophys. Res. **105**, 21,081 (2000)
6. J. A. Fedder, J. G. Lyon: J. Geophys. Res. **100**, 3623 (1995)
7. S. Cable, R. S. Steinolfson: J. Geophys. Res. **100**, 21,645 (1995)
8. H. Washimi, T. Tanaka: Space Sci. Rev. **78**, 85 (1996)
9. T. Tanaka, K. Murawski: J. Geophys. Res. **102**, 19,805 (1997)
10. T. J. Linde, T. I. Gombosi, P. L. Roe, G. Powell, D. L. DeZeeuw: J. Geophys. Res. **103**, 1889 (1998)
11. T. Tanaka, H. Washimi: J. Geophys. Res. **104**, 12,605 (1999)
12. G. L. Siscoe, N. U. Crooker, G. M. Erickson, B. U. O. Sonnerup, K. D. Siebert, D. R. Weimer, W. W. White, N. C. Maynard: 'Global geometry of magnetospheric currents'. In: *Magnetosperic Current System*, ed. by S. I. Ohtani (AGU, Washington D.C. 2000) pp. 41-52
13. M. Vinokur: J. Comput. Phys. **82**, 1 (1989)
14. M. Brio, C. C. Wu: J. Comput. Phys. **75**, 400 (1988)
15. T. Tanaka: Comp. Fluid Dyn. J. **1**, 14 (1992)
16. T. Tanaka: SIMPO Newsl. **3**, 31 (1993)
17. B. van Leer: J. Comput. Phys. **32**, 101 (1979)
18. H. C. Yee, G. H. Klopfer, J. L. Montagne: J. Comput. Phys. **88**, 31 (1990)
19. T. Tanaka: J. Comput. Phys. **111**, 382 (1994)
20. K. Murawski, T. Tanaka: Astrophys. Space Sci. **25**4, 187 (1997)
21. J. Brackbill, D. Barnes: J. Comput. Phys. **35**, 426 (1980)
22. E. N. Parker: *Interplanetary Dynamical Processes* (Interscience, New York 1963)
23. H. Washimi, T. Tanaka: Adv. Space Res. **23(3)**, 551 (1999)
24. T. Tanaka: Earth Planets Space **50**, 259 (1998)
25. T. Tanaka: Adv. Space Res. **26(10)**, 1577 (2000)
26. T. Tanaka: 'Generation mechanism of the field-aligned current system deduced from a 3-D MHD simulation of the solar wind-magntosphere-ionosphere coupling'. In: *Magnetospheric Research with Advanced Techniques*. ed. by R. L. Xu, A. T. Y. Lui (Pergamon, 1998) pp. 133-142